analytical chemistry

pubs.acs.org/ac Article

A Target-Driven Self-Feedback Paper-Based Photoelectrochemical Sensing Platform for Ultrasensitive Detection of Ochratoxin A with an In_2S_3/WO_3 Heterojunction Structure

Xiaoran Tan, Haihan Yu, Bing Liang, Mengting Han, Shenguang Ge, Lina Zhang, Lin Li, Li Li,* and Jinghua Yu*

Cite This: *Anal. Chem.* 2022, 94, 1705−1712 Read Online

ACCESS | Metrics & More | Article Recommendations | Supporting Information

ABSTRACT: Currently, developing versatile, easy-to-operate, and effective signal amplification strategies hold great promise in photoelectrochemical (PEC) biosensing. Herein, an ultrasensitive polyvinylpyrrolidone-treated In_2S_3/WO_3 (In_2S_3-P/WO_3)-functionalized paper-based PEC sensor was established for sensing ochratoxin A (OTA) based on a target-driven self-feedback (TDSF) mechanism enabled by a dual cycling tactic of PEC chemical−chemical (PECCC) redox and exonuclease III (Exo III)-assisted complementary DNA. The In_2S_3-P/WO_3 heterojunction structure with 3D open-structure and regulable topology was initially in situ grown on Au nanoparticle-functionalized cellulose paper, which was served as a universal signal transducer to directly record photocurrent signals without complicated electrode modification, endowing the paper chip with admirable anti-interference ability and unexceptionable photoelectric conversion efficiency. With the assistance of Exo III-assisted cycling process, a trace amount of OTA could trigger substantial signal reporter ascorbic acid (AA) generated by the enzymatic catalysis of alkaline phosphatase, which could effectively provoke the PECCC redox cycling among the tris(2-carboxyethyl)phosphine acid, AA, and ferrocenecarboxylic at the In_2S_3-P/WO_3 photoelectrode, initiating TDSF signal amplification. Based on the TDSF process induced by the Exo III-assisted recycling and PECCC redox cycling strategy, the developed paper-based PEC biosensor realized ultrasensitive determination of OTA with persuasive selectivity, high stability, and excellent reproducibility. It is believed that the proposed paper-based PEC sensing platform exhibited enormous potential for the detection of other targets in bioanalysis and clinical diagnosis.

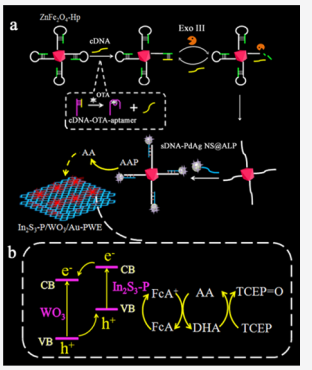

INTRODUCTION

Ochratoxin A (OTA), a prevalent toxic mycotoxin and substantial burden on the humans' healthcare, is normally present in an extensive variety of products, including corn, wheat, wine, coffee, and beer.[1,2] In view of its highly hepatotoxic, nephrotoxic, teratogenic, and mutagenic properties to most mammalian species, OTA is considered as a potential carcinogen (Group 2B) by the International Agency for Research on Cancer.[3−5] Nowadays, many techniques including mass spectroscopy,[6] high-performance chromatography,[7] and antibody-based techniques[8] have been developed for OTA detection. There is no doubt that these methods possess great advantages, yet they still suffer from elaborate instrumentation, professional technical operation, and high running cost, which inevitably limit their applications. Thus, it is of great significance to explore rapid, low-cost, and sensitive equipment for the detection of OTA.

Nowadays, newly emerging microfluidic paper-based analytical devices (μPAD), with merits of multifunctionality, satisfactory bendability, and admirable biocompatibility, have achieved enormous progress in the fields of manufacturing environment, clinical diagnostics, and so forth.[9−15] Among them, paper-based photoelectrochemical (PEC) bioassay, combining plenty of excellent performances of PEC bioanalysis and cellulose paper, has attracted extensive attention because of its portability, high sensitivity, and low background.[16−18] In the quest for effectively improving PEC performance, ideal photoactive materials, as one of the most complicated and crucial factors, have been actively pursued among the field.[19,20] Tungsten trioxide (WO_3) is seen as a promising n-type semiconductor owing to its attractive features including high carrier mobility, wide-range spectral absorption, and eminent chemical stability,[21−23] which exhibits great potential to be an excellent photoactive material. However, the application of unmodified WO_3 is restricted due to the weakness of its wide band gap of 2.6−2.8 eV and the high recombination rate of electron−hole pairs, which hinders the efficient conversion from photo to electricity.[24,25] Therefore, selecting a sensitizer

Received: September 30, 2021
Accepted: December 30, 2021
Published: January 11, 2022

https://doi.org/10.1021/acs.analchem.1c04259
Anal. Chem. 2022, 94, 1705−1712

with prominent sensitization efficiency for WO_3 is critical to accelerate the photo-electric conversion. As a desirable signal enhancer for optimizing photo-generated carrier separation, In_2S_3 has intense optical absorption in the visible region and its band gap (2.25 eV) matches perfectly with that of WO_3,[26,27] making it an excellent photoactive material to sensitize WO_3. The prepared In_2S_3/WO_3 sensitization structure with a staggered band alignment is expected to promote the bulk carrier separation of WO_3 and acquire an extraordinary initial photocurrent response.

To further improve detection sensitivity of the paper-based PEC biosensor, developing a simple yet effective signal amplification strategy is also essential. Specially, the PEC chemical−chemical (PECCC) redox cycling amplification (RCA) strategy, a prevalent technique involving continuously coupled oxidation−reduction reactions, has been testified as an available measure for signal amplification,[28−32] which is destined to impact the PEC biosensor to extra merits of unsophisticated fabrication, short time consumption, as well as exceedingly good stability and reproducibility in practical applications. However, the amplification efficiency still seems unsatisfactory since each target could only be converted into a small quantity of signal indicators for PEC immunoassay in reported works.[28,29] Accordingly, it is useful to design a novel target-driven self-feedback (TDSF) strategy constructed by the integration of an exonuclease III (Exo III)-assisted cycle amplification route and RCA, which can realize a high target-to-signal indicator conversion ratio, further enhancing the amplification efficiency. To our knowledge, such an ultrasensitive dual recycling amplification strategy has so far not yet been unleashed.

Herein, a simple and ultrasensitive paper-based PEC biosensor was designed for detecting OTA based on the polyvinylpyrrolidone (PVP)-treated In_2S_3/WO_3 (In_2S_3-P/WO_3) composites' coupling with the Exo III-assisted recycling and RCA strategy. The In_2S_3-P/WO_3 heterostructure has been successfully synthesized on a Au nanoparticle (AuNP)-functionalized cellulose paper electrode (Au-PWE), leading to photocurrent amplification by inducing sulfur vacancies and gradient oxygen doping into In_2S_3. Specifically, $ZnFe_2O_4$ octahedrons were employed for the immobilization of a hairpin probe (Hp) and magnetic separation. With the existence of OTA, complementary DNA (cDNA) released from double-stranded DNA (dsDNA1) (OTA-aptamer/cDNA complex) hybridized with Hp to form dsDNA2 (Hp/cDNA duplex). Then Exo III would digest dsDNA2, releasing cDNA to further trigger next cycling amplification. The residual short single-stranded DNA (ssDNA) on the surface of $ZnFe_2O_4$ octahedrons could recognize signal DNA (sDNA)-labeled PdAg nanospheres (PdAgNSs) with alkaline phosphatase (ALP) decoration to generate $ZnFe_2O_4$ octahedrons/dsDNA3/PdAgNSs@ALP assemblies. Accompanying the Exo III-assisted cycling process, a large number of DNA nanoassemblies was fabricated (Scheme 1a). As depicted in Scheme 1b, the signal indicator ascorbic acid (AA) was generated steadily and updated procedurally by enzymatic conversion of ascorbic acid 2-phosphate (AAP) by sDNA-PdAgNSs@ALP and recirculation of the PECCC redox between ferrocenecarboxylic acid (FcA) and tris(2-carboxyethyl) phosphine (TCEP). Such a multiple-signal amplification and immobilization-free process avoided the interference of layer-by-layer modification on electrodes and dramatically improved the detection sensitivity. This high-efficiency and exclusive work is expected to pave a new avenue for design and development of high-performance paper-based PEC biosensor.

Scheme 1. (a) Schematic Illustration of Enzyme-Assisted Recycling Amplification Process and (b) PECCC RCA on In_2S_3-P/WO_3/Au-PWE

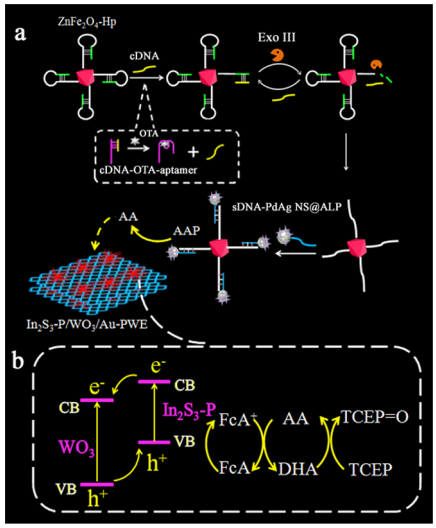

EXPERIMENTAL SECTION

Preparations of In_2S_3-P/WO_3/Au-PWE. Figure S1 displayed the fabrication of a PEC paper analytical device, which was operated by combining wax printing with AuNPs functionalization (details are given in the Supporting Information). Then, 0.116 g of sodium tungsten dehydrate ($Na_2WO_4{\cdot}2H_2O$) was dropped into 15 mL of deionized water and kept being stirred for several minutes. Subsequently, 4 mL of 3.0 M HCl and 0.1 g of ammonium oxalate ($(NH_4)_2C_2O_4$) were added into the solution, followed by introducing 15 mL of ultrapure water with continuous stirring for 30 min. The cleaned Au-PWE substrate with the conductive side facing down was placed into a Teflon-lined stainless steel autoclave, and the as-prepared precursor solution was added into the autoclave. The hydrothermal reaction was carried out at 140 °C for 2 h. After washing with deionized water and cooling down to room temperature, the yellow-colored WO_3/Au-PWE was acquired. To obtain the In_2S_3 nanosheet-coated WO_3/Au-PWE, 250 mg of thioacetamide and 700 mg of citric acid were dissolved in 50 mL of 0.015 M $InCl_3$ solution. The water bath process was performed by immersing WO_3/Au-PWE in In_2S_3 precursor solution at 80 °C lasting for 2.5 h. After that, the In_2S_3/WO_3/Au-PWE sample was placed into 10^{-3} g mL^{-1} PVP aqueous solution and finally dried at 60 °C in air.

Preparation of $ZnFe_2O_4$ Octahedrons. The $ZnFe_2O_4$ octahedrons were synthesized by a one-step hydrothermal method.[33] Briefly, 0.35 g of $Zn(OAc)_2{\cdot}2H_2O$, 1 g of $FeSO_4{\cdot}7H_2O$, and 5 mL of 10 M $N_2H_4{\cdot}H_2O$ were put in 40 mL of deionized water under vigorous stirring. The precursor solution was introduced into a Teflon autoclave, which was maintained at 180 °C for 14 h before the solution was gradually cooled back to room temperature. Afterward, the precipitate was accumulated by filtration and repeatedly washed with distilled water and ethanol in sequence. Finally, the magnetic octahedrons were dried at 60 °C overnight.

Preparation of PdAg Nanospheres. To prepare PdAg nanospheres, 2 mM dioctadecyldimethylammonium chloride

https://doi.org/10.1021/acs.analchem.1c04259
Anal. Chem. 2022, 94, 1705−1712

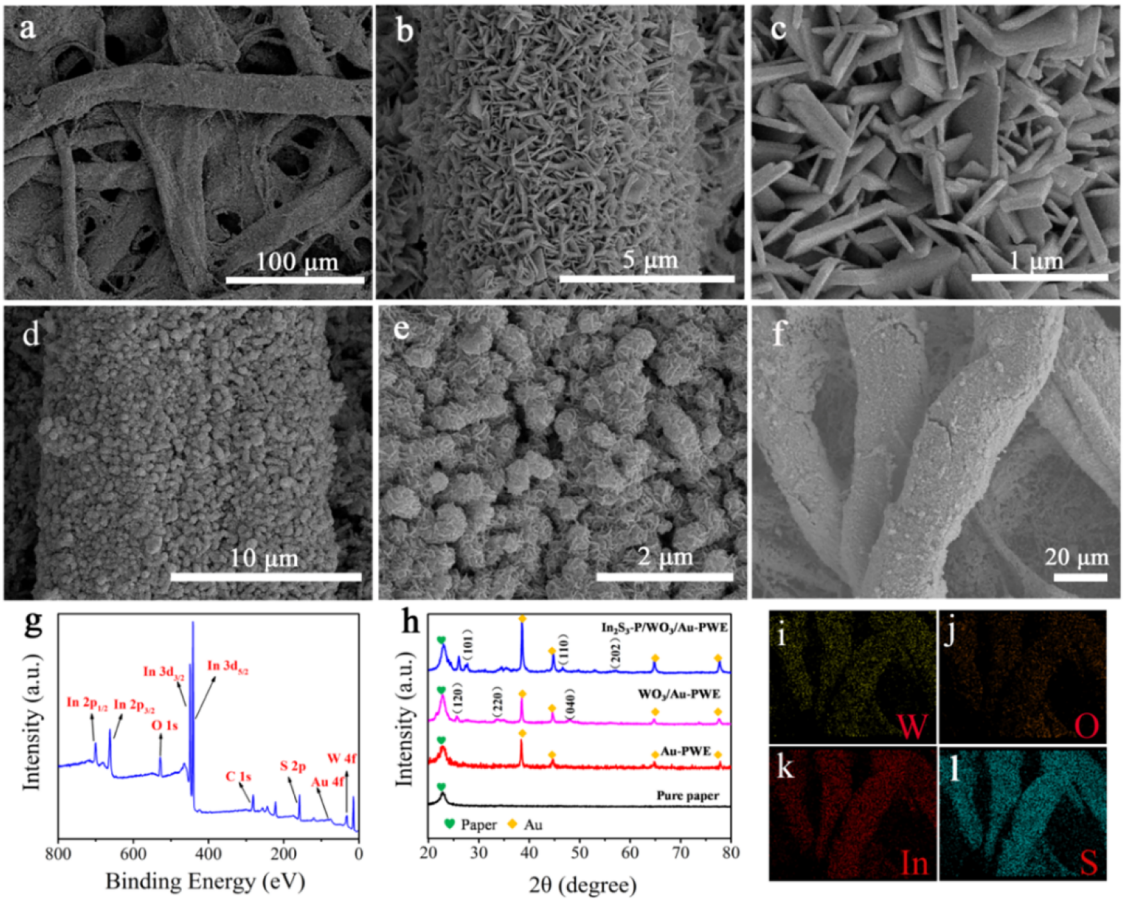

Figure 1. SEM images of the (a) Au-PWE, (b, c) WO_3/Au-PWE, (d, e) In_2S_3/WO_3/Au-PWE, and (f) In_2S_3-P/WO_3/Au-PWE. The XPS survey spectrum of (g) the In_2S_3-P/WO_3/Au-PWE. (h) XRD patterns of pure paper, Au-PWE, WO_3/Au-PWE, and In_2S_3-P/WO_3/Au-PWE. (i–l) Elemental mapping of the In_2S_3-P/WO_3/Au-PWE.

(DODAC) and 20 mL of deionized water were added in a flask and heated to 60 °C. Next, 0.668 mL of 10 mM $AgNO_3$ and 1.334 mL of 10 mM H_2PdCl_4 were poured into the obtained solution immediately.[34] The solution could create insoluble black precipitate with the dropwise addition of 2 mL of 0.3 M ascorbic acid, triggering the co-reduction of Pd and Ag. After reacting for 30 min, the black solid product was harvested by centrifugation, followed by washing with isopropanol and water several times, and finally lyophilized.

Synthesis of sDNA-PdAgNSs@ALP. The prepared PdAg nanospheres (10 mg) were dissolved into 2 mL of phosphate-buffer saline (PBS) (pH 7.5). Then, 100 μL of ALP (1 mg mL^{-1}) was added into a PdAg nanosphere solution and stirred for 12 h under 4 °C. As a result, PdAgNS was decorated with ALP to form PdAgNS@ALP by the covalent bonding between PdAgNS and $-NH_2$ in ALP. Subsequently, the solution was centrifuged to remove unconjugated ALP and then dispersed in 2 mL of PBS. After centrifugation and washing, PdAgNS@ALP was redispersed in 2 mL of PBS and kept at 4 °C for future use. Sulfhydryl-modified sDNA (10 μM, 7.5 μL) was modified on the surface of PdAgNS@ALP (100 μL) through the chemical force between the sulfhydryl group and PdAg at 37 °C for 12 h. After that, 400 μL of 1.0% (w/v) BSA was used to block the nonspecific binding sites for 1 h at 37 °C. Then, sDNA-PdAgNS@ALP was gained by centrifuging and washing, and the supernatant was removed.

Immobilization of the Hp on the Surfaces of $ZnFe_2O_4$ Octahedrons. An amino-modified Hp (NH_2-Hp) (10 μM, 15 μL) was attached to the surface of $ZnFe_2O_4$ octahedrons (100 μL) with soft swaying at 37 °C for 3 h owing to the strong interaction between $-COOH$ and $-NH_2$. Finally, Hp-labeled $ZnFe_2O_4$ octahedrons were dispersed in 100 μL of tris buffer.

Construction of the PEC Biosensor. The fabrication process of the PEC sensor is illustrated in Scheme 1. Briefly, 5 μL of OTA-aptamer (2 μM) and cDNA (2 μM) were added into a tube for 1 h at 37 °C to form dsDNA1. Then, dsDNA1 was dropped into 5 μL of OTA standard solution with varied concentrations, for 1.5 h at a temperature of 37 °C to release cDNA. After the addition of as-prepared Hp-modified $ZnFe_2O_4$ octahedrons (25 μL), the released cDNA hybridized with Hp to form dsDNA2. Exo III (1 μL, 20 U μL^{-1}) would digest the 3′-end of the Hp in dsDNA2 at 37 °C for 100 min, releasing cDNA and leaving a short ssDNA on the $ZnFe_2O_4$ octahedrons surface. The output cDNA was further captured by the Hp for 2 h at 37 °C to accomplish cycling amplification. Then, the sDNA on the PdAgNS@ALP surface would match with the remaining ssDNA incubated at 37 °C for 6 h to generate $ZnFe_2O_4$ octahedrons/dsDNA/PdAgNS@ALP nanoassemblies. Subsequently, the nanoassemblies were collected through magnetic separation. After that, the $ZnFe_2O_4$ octahedrons/dsDNA/PdAgNS@ALP was allowed to incubate with 1.0 mM AAP at 37 °C for 1 h. The enzymatic product (AA) of ALP was dropped into the working zone of the paper electrode containing 0.3 mM FcA and 0.4 mM TCEP.

https://doi.org/10.1021/acs.analchem.1c04259
Anal. Chem. 2022, 94, 1705−1712

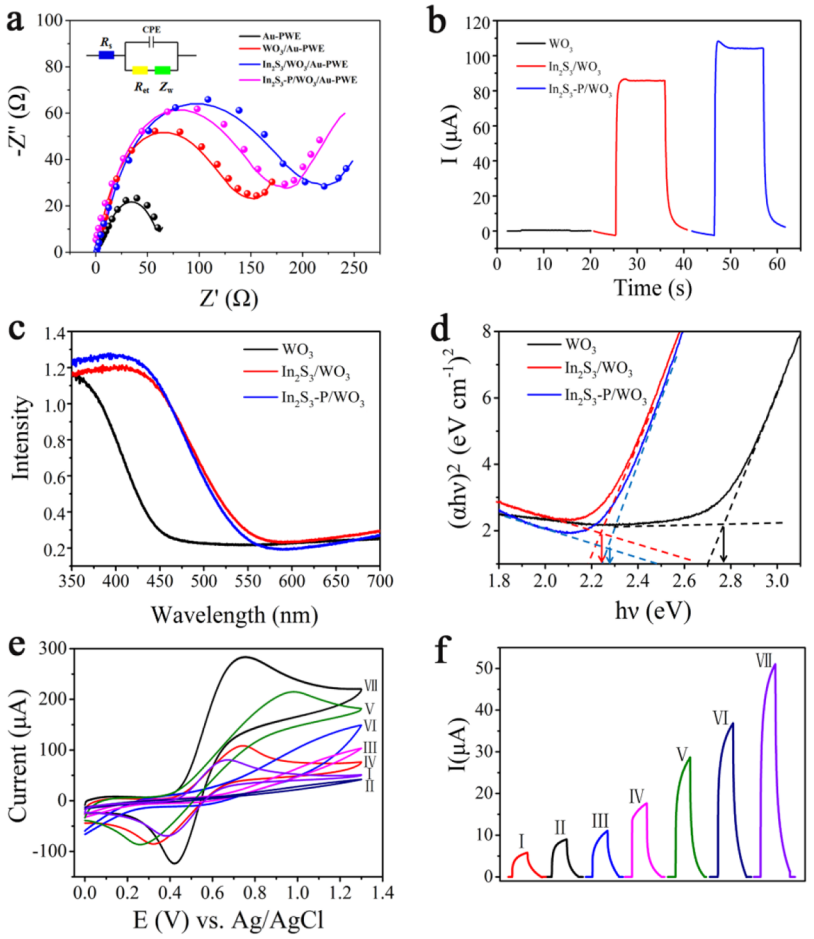

Figure 2. (a) EIS of the Au-PWE, WO_3/Au-PWE, In_2S_3/WO_3/Au-PWE, and In_2S_3-P/WO_3/Au-PWE in PBS (pH 7.4, 0.1 M) containing 5.0 mM $[Fe(CN)_6]^{3-/4-}$. (b) PEC responses (in 0.1 M Na_2SO_4 solution), (c) the UV−vis diffuse reflectance spectra, and (d) Tauc plots of the WO_3/Au-PWE, In_2S_3/WO_3/Au-PWE, and In_2S_3-P/WO_3/Au-PWE. (e) CV curves of the Au-PWE and (f) photocurrent of the In_2S_3-P/WO_3/Au-PWE in varied tris buffer solutions (from I to VII: FcA, AA, TCEP, FcA/TCEP, FcA/AA, TCEP/AA, and FcA/AA/TCEP). The concentrations of FcA, AA, and TCEP are 0.3, 0.2, and 0.4 mM, respectively.

RESULTS AND DISCUSSION

Characterizations of the Prepared Nanomaterial. The gradual synthesis process of the In_2S_3-P/WO_3/Au-PWE was characterized by scanning electron microscopy (SEM), which is shown in Figure 1a−f. For endowing the insulated paper fibers with superior conductivity, uniform Au NPs were densely decorated onto the surface of cellulose paper (Figure 1a). According to Figure 1b,c, orderly arranged WO_3 nanosheets with a regular plate-like structure were uniformly distributed onto the Au-PWE by a simple hydrothermal process. Figure 1d,e showed that In_2S_3 ultrathin nanoflakes were further grown onto the surface of the WO_3/Au-PWE, resulting in an In_2S_3/WO_3 core−shell heterostructure. Immersing the In_2S_3/WO_3/Au-PWE in PVP solution at 90 °C for 3 h, the morphological characteristic of the In_2S_3-P/WO_3/Au-PWE (Figure 1f) did not change significantly compared with that of the untreated sample (Figure S2). In Figure 1i−l, elemental mapping results demonstrated that W, O, In, and S elements were immobilized on the Au-PWE, attesting the successful fabrication of the In_2S_3-P/WO_3/Au-PWE. X-ray photoelectron spectroscopy (XPS) analysis was further conducted to measure the surface chemical compositions of the In_2S_3-P/WO_3/Au-PWE. As illustrated in Figure 1g, these peaks proved the presence of Au, W, O, In, and S elements. The high-resolution XPS spectra of W 4f, O 1s, In 3d, and S 2p were also obtained as displayed in Figure S3. The peaks of W 4f (32.3 and 35.0 eV), O 1s (528.0 eV), In 3d (441.0 and 449.4 eV), and S 2p (157.7 and 159.3 eV) certified the existence of W^{6+}, O^{2-}, In^{3+}, and S^{2-} in the heterojunction, respectively.

X-ray diffractometry (XRD) was applied to investigate the surface modification process of the In_2S_3-P/WO_3/Au-PWE. As described in Figure 1h, apart from the diffraction peaks belonging to cellulose and face-centered cubic gold, the XRD patterns of the WO_3/Au-PWE displayed three additional diffraction peaks at 26.6, 34.0, and 48.4°, which were assigned to the (120), (220), and (040) crystal planes of cubic WO_3 (JCPDS 20-1324). After the growth of In_2S_3 and efficient treatment of PVP, the obvious diffraction peaks observed from the XRD patterns of In_2S_3 could be assigned to (101), (110), and (202) planes of In_2S_3 (JCPDS 33-0623). Those results confirmed that In_2S_3-P/WO_3/Au-PWEs were successfully prepared.

Characterization of the $ZnFe_2O_4$ Octahedrons and PdAgNSs. The $ZnFe_2O_4$ octahedrons as the magnetic materials were used to immobilize the Hp and realize magnetic separation under the action of the magnetic field. The morphologies and structures of $ZnFe_2O_4$ octahedrons were characterized by SEM. As shown in Figure S4a, the product

https://doi.org/10.1021/acs.analchem.1c04259
Anal. Chem. 2022, 94, 1705−1712

was formed with numerous of symmetrical and smooth octahedrons with uniform size in the range from 100 to 350 nm. The infrared spectrum of $ZnFe_2O_4$ octahedrons is given in Figure S4b. The peak observed at 1382 cm^{-1} corresponded to the in-plane bending vibration of O−H, while the band at 1645 cm^{-1} was ascribed to the existence of carbonyl groups (C═O). The peak displayed at around 1104 cm^{-1} was attributed to the C−O stretching mode. These data indicated that the as-prepared $ZnFe_2O_4$ octahedrons were surrounded by −COOH groups. Elemental mapping analysis (Figure S4c) and the energy-dispersive spectrometry (EDS) image (Figure S4d) revealed that there were Zn, Fe, and O elements in the obtained product, indicating the successful preparation of $ZnFe_2O_4$.

Transmission electron microscopy (TEM) was carried out to explore the morphological characteristics of the prepared PdAgNSs. As illustrated in Figure S5a, the PdAg material was discovered to be composed of 3D hollow nanoparticles with an average radius of 30 nm. In particular, these nanoparticles had a distinctive dendritic structure radiating from the center of the sphere. To further investigate the hybrid compositions of PdAgNSs, their crystal structures were validated by X-ray diffraction (XRD) patterns. Their diffraction peaks were located between the corresponding peaks of pure Ag and pure Pd, proving the successful formation of PdAg nanospheres (Figure S5b).

Feasibility of the Proposed Paper-Based PEC Biosensor. The stepwise fabrication of the In_2S_3-P/WO_3/Au-PWE was first characterized based on electrochemical impedance spectroscopy (EIS) measurements in 5.0 mM $[Fe(CN)_6]^{3-/4-}$. In the EIS Nyquist plots, the diameter of the semicircle directly showed electron transfer resistance (R_{et}). As expected, the Au-PWE obtained a smaller semicircle (black line, R_{et} = 59.73 Ω) owing to the high conductivity. With the modifications of WO_3 (red line, R_{et} = 145.4 Ω) and In_2S_3 (blue line, R_{et} = 194.7 Ω), the R_{et} increased step by step due to the poor conductivity of semiconductors. The PVP-treated In_2S_3/WO_3/Au-PWE showed a smaller semicircle diameter (pink line, R_{et} = 180.2 Ω) compared with that of the pristine In_2S_3/WO_3/Au-PWE, demonstrating that gradient oxygen doping brought lower transport resistance and facilitated the interface charge transfer. Figure 2b compares the PEC performances of the WO_3/Au-PWE, In_2S_3/WO_3/Au-PWE, and In_2S_3-P/WO_3/Au-PWE in 0.1 M Na_2SO_4 solution. For the WO_3/Au-PWE, the photocurrent intensity was hardly observed due to the fast recombination of electron−hole pairs on the WO_3 surface, whereas the In_2S_3/WO_3/Au-PWE generated large photocurrent benefiting from the band matching of the heterojunction. Significantly, the In_2S_3-P/WO_3/Au-PWE presented a much stronger signal, which is mainly attributed to sulfur vacancies and gradient oxygen doping into In_2S_3 caused by the PVP treatment. The UV−vis absorption spectrum of the WO_3/Au-PWE (Figure 2c) has a wavelength threshold at about 450 nm, while the integration of In_2S_3 nanosheets improved the absorption of WO_3 in a long-wavelength region. In addition, the same absorption edge between the In_2S_3/WO_3/Au-PWE and In_2S_3-P/WO_3/Au-PWE indicated that light absorption was affected slightly by the treatment of PVP. The band gap energies (E_g) of the WO_3/Au-PWE, In_2S_3/WO_3/Au-PWE, and In_2S_3-P/WO_3/Au-PWE were estimated by the Tauc plots, which were determined to be 2.76, 2.24, and 2.26 eV (Figure 2d), respectively.[35] Those results confirmed that the formation of a heterojunction caused effective carrier separation and increased the visible light utilization, which made it possible to significantly improve the photoelectric conversion efficiency.

Cyclic voltammetry (CV) curves of the Au-PWE in various tris buffer solutions were employed to validate the feasibility of PECCC RCA (Figure 2e). Compared with the CV curves of AA (curve II) and TCEP (curve III), an enhanced oxidation peak of FcA (curve I) was detected at ∼0.63 V, indicating that FcA was more easily oxidized than both TCEP and AA. Moreover, for the FcA/TCEP system, the narrow oxidation peak with lower current intensity showed that the FcA could not be regenerated by TCEP (curve IV). For the FcA/AA system, the much higher peak current proved that the oxidative product FcA could be regenerated from FcA^+ by a small portion of AA (curve V). Also, the coexistence of TCEP and AA accelerated the regeneration of AA over a broad potential range (curve VI). As shown in curve VII, the highest photocurrent signal was produced in the FcA/AA/TCEP system, verifying that the presence of three electron donors initated running of RCA.

The PEC performance of the In_2S_3-P/WO_3/Au-PWE with different solution treatments was tested. All photocurrent signals we detected showed a curved shape in the first nearly 150 s, and the current gradually reached a stable status after 150 s of the test. When the testing time was prolonged by 30 s, the photocurrent intensity could reach a stable value (Figure S7). Therefore, in order to obtain fast and accurate detecting results, the photocurrent measured from 60 to 70 s was selected as the optimum PEC response result for further analysis (the mechanism is described in the Supporting Information). As illustrated in Figure 2f, it was apparent that the photoelectrode treated with FcA (curve I), AA (curve II), and TCEP (curve III) solutions generated obvious photocurrent responses. This is because the three substances could be oxidized by the photogenerated holes of the In_2S_3-P/WO_3/Au-PWE, which realized the efficient separation of photogenerated carriers. Furthermore, since the FcA could not be regenerated by TCEP, a slight photocurrent signal enhancement was observed in the presence of FcA and TCEP (curve IV). In the AA/TCEP system, the photoelectric signal improvement revealed that the existence of TCEP contributed to the regeneration of AA (curve V). Similarly, the regeneration of FcA from the reaction between FcA^+ and AA could cause a much higher signal of FcA (curve VI). For FcA, AA, and TCEP systems, an obviously increased photocurrent response was obtained (curve VII), which performed the largest enhancement in these comparison systems. It was distinctly manifested that the as-expected signal amplification effect of the RCA strategy was achieved on the basis of the In_2S_3-P/WO_3/Au-PWE, which had great potential for improving the sensitivity of the bioanalysis.

Polyacrylamide Gel Electrophoresis (PAGE) Characterization. OTA-aptamer, cDNA, Hp, and sDNA were precisely designed, and the generated products of the Exo III-assisted cycle process were analyzed by PAGE to verify its rationality. As displayed in Figure 3, lanes 1 to 4 individually corresponded to the four DNA strands. When OTA was introduced into equivalent amounts of OTA-aptamer and cDNA, there was a new band with high molecular weight appearing at the top of lane 5, suggesting that the dsDNA1 was generated. Moreover, a significant cDNA band was observed in lane 5, confirming that dsDNA1 released cDNA in the presence of OTA. After the introduction of Hp and Exo III, a

https://doi.org/10.1021/acs.analchem.1c04259
Anal. Chem. 2022, 94, 1705−1712

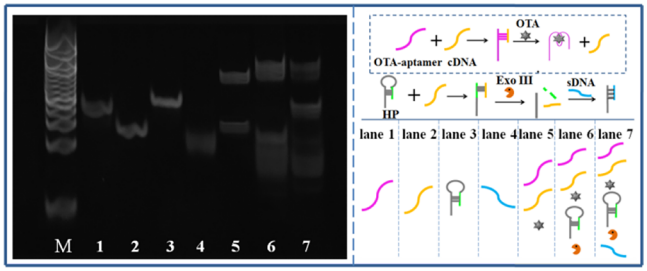

Figure 3. Native PAGE characterization for the Exo III-assisted cyclic amplification strategy. Lane M: DNA marker (10−150 bp); lane 1: OTA-aptamer (6 μL, 10 μmol L^{-1}); lane 2: cDNA (6 μL, 10 μmol L^{-1}); lane 3: Hp (6 μL, 10 μmol L^{-1}); lane 4: sDNA (6 μL, 10 μmol L^{-1}); and lane 5: OTA-aptamer + cDNA (6 μL, 10 μmol L^{-1}) + OTA (0.5 μL, 0.1 ng mL^{-1}); lane 6: products of lane 5 after the addition of Hp and Exo III (20 U); and lane 7: products of lane 6 after the addition of sDNA.

few new stripes with various high and low molecular weights appeared and formed a sliding zone, which indicated that the released cDNA hybridized with the Hp to form dsDNA2, and Exo III would gradually digest the 3′-end of the Hp in the dsDNA2 to release cDNA, leaving a short ssDNA. A new band appeared in the middle of lane 7 when sDNA was added to the system, indicating that sDNA could hybridize with the left short ssDNA to form dsDNA3. These results successfully demonstrated the rationality of the designed four DNA strands and the Exo III-assisted cyclic amplification strategy.

Feasibility Test and Optimization of the Reaction Conditions. Figure 4a exhibited the effect of concentration variation of FcA to PECCC redox cycling on the In_2S_3-P/WO_3/Au-PWE. The experimental results clearly demonstrated that 0.3 mM displayed the strongest PEC signal amplification. As shown in Figure 4b, when the concentration of TCEP to PECCC redox cycling on the In_2S_3-P/WO_3/Au-PWE was 0.4 mM, the maximum PEC signal was obtained. Thus, 0.3 mM FcA and 0.4 mM TCEP were chosen for the following experiment. Figure S6a−c illustrated the incubation time optimization of the Exo III-assisted recycling process (the detailed description is shown in the Supporting Information). As shown in Figure 4c,d, without the addition of Exo III or ALP in the system, the detection sensitivity of OTA (10^{-8} g mL^{-1}) was greatly reduced, which verified the necessity of these two enzymes in synergistically promoting photocurrent. Moreover, in order to explore the influence of different substrate compositions on the sensitivity of the sensor, contrast experiments were conducted by comparing photoelectric responses to OTA detection (0, 10^{-10}, and 10^{-9} g mL^{-1}) of the In_2S_3-P/WO_3/Au-PWE to those of WO_3/Au-PWE, In_2S_3/Au-PWE, and In_2S_3/WO_3/Au-PWE under the optimized conditions. As shown in Figure 4e,f, the sensors with the WO_3/Au-PWE and In_2S_3/Au-PWE only gave inconspicuous photocurrent signal changes for OTA compared with the blank sample. However, the sensor with the In_2S_3/WO_3/Au-PWE and In_2S_3-P/WO_3/Au-PWE showed a dramatic increase of photocurrent after the addition of OTA, and the latter gave a more sensitive photoelectric response (Figure 4g,h).

PEC Detection of OTA. The sensitivity of the paper-based PEC biosensor was evaluated by adding various concentrations of the OTA standard solution. After multiple parallel experiments, it has been found that the trend of $I-t$ curves of target detection is the same as that in Figure S7. Consequently, the photocurrent signals in Figure 5a were uniformly selected from 60 to 70 s, representing the average height and rapid detection result. As shown in Figure 5a, the photocurrent intensity of the paper-based PEC sensor increased with increasing concentrations of targets due to more OTA promoting the PECCC RCA. The photocurrent intensity had an ideal linear relationship with the logarithm of OTA concentration in the range from 10^{-13} to 10^{-7} g mL^{-1} (Figure 5b). In addition, the corresponding low limit of detection (LOD) was estimated to be 0.052 pg mL^{-1} (S/N = 3), which follows the correlation equation I = 84.88 + 5.62 lg c_{OTA} (R^2 = 0.996). The performance comparison of different

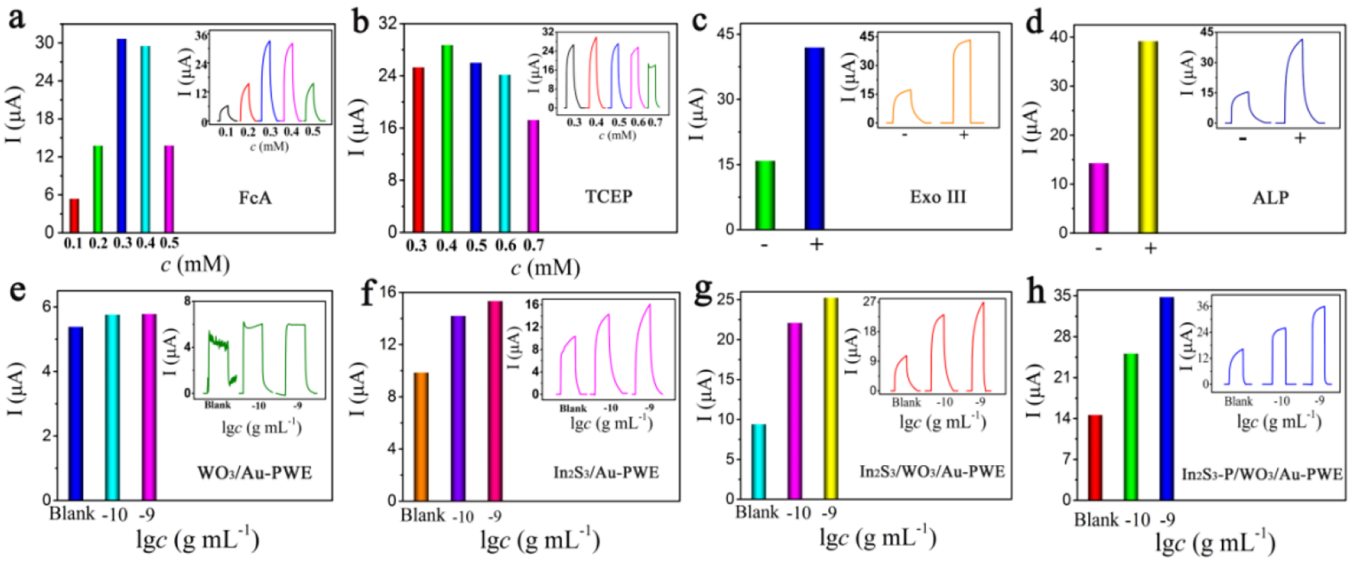

Figure 4. PEC response of the In_2S_3-P/WO_3/Au-PWE in tris buffer solution containing (a) 0.4 mM TCEP and 0.2 mM AA with different concentrations of FcA from 0.1 to 0.5 mM and (b) 0.2 mM AA and 0.3 mM FcA with different concentrations of TCEP from 0.3 to 0.7 mM. (c, d) Photocurrent curves of the aptasensor for OTA incubated without or with (c) Exo III or (d) ALP. PEC tests of the proposed sensor incubated with different concentrations of OTA (0, 10^{-10}, and 10^{-9} g mL^{-1}) using different electrodes: (e) WO_3/Au-PWE, (f) In_2S_3/Au-PWE, (g) In_2S_3/WO_3/Au-PWE, and (h) In_2S_3-P/WO_3/Au-PWE.

https://doi.org/10.1021/acs.analchem.1c04259
Anal. Chem. 2022, 94, 1705−1712

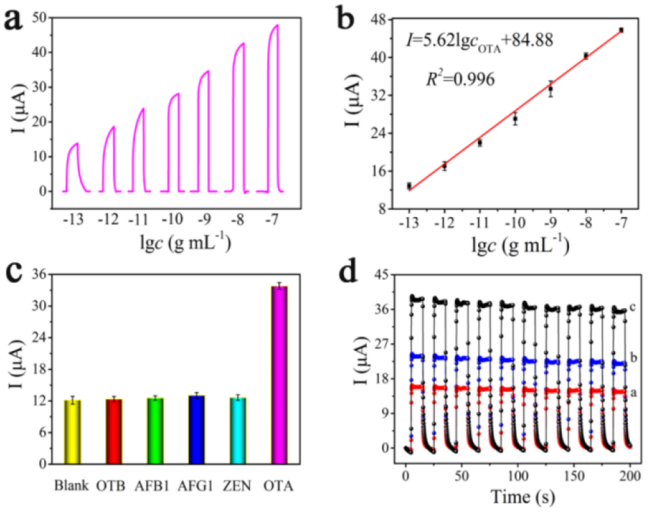

Figure 5. (a) PEC response of the sensor to different target concentrations. (b) As-derived linear curve. (c) Specificity of the prepared PEC aptasensor against 10^{-8} g mL^{-1} OTB, 10^{-8} g mL^{-1} AFB1, 10^{-8} g mL^{-1} AFG1, 10^{-8} g mL^{-1} ZEN, and 10^{-9} g mL^{-1} target OTA, and (d) the stability test of the electrode with the OTA concentrations of 10^{-12} (curve a), 10^{-10} (curve b), and 10^{-8} g mL^{-1} (curve c).

analytical methods for OTA detection (Tables S1 and S2) demonstrated that this strategy owned a lower LOD and comparable slope of linear range. The results indicated the remarkable performances of the developed paper-based PEC sensing platform.

Specificity and Potential Application of the Proposed PEC Biosensor. To value the specificity of the devised PEC biosensor, some relevant interfering species at 10-fold higher concentrations compared with that of OTA (10^{-9} g mL^{-1}), including ochratoxin B (OTB), aflatoxin B1 (AFB1), aflatoxin G1 (AFG1), and zearalenone (ZEN), were employed to execute experiments for comparison. As depicted in Figure 5c, an apparent photocurrent signal was obtained with the appearance of OTA; nevertheless, other interfering mycotoxins had no effect on the photocurrent. These detection consequences of 10-fold interferences were similar to the blank test, indicating that the designed PEC biosensor owned admirable anti-interference ability and high specificity. The detection of OTA in foodstuff further verified the applicability of this proposed aptasensor, and the results are summarized in Table S3. In order to evaluate the stability of the PEC sensor, we selected the detecting signal after 150 s, which was more flat and representative. As shown in Figure 5d, after 10 consecutive light on-and-off cycles, the signal response of this PEC bioanalysis showed a negligible change with OTA concentrations of 10^{-12}, 10^{-10}, and 10^{-8} g mL^{-1}, respectively, indicating that the designed strategy owned excellent stability.

CONCLUSIONS

In summary, a novel ultrasensitive TDSF paper-based PEC aptasensor for the detection of OTA was established based on an In_2S_3/WO_3-sensitized heterojunction structure and a dual cycling amplification strategy. The photosensitive heterostructure of the In_2S_3-P/WO_3/Au-PWE represented outstanding photoelectric performance relying on type II band alignment and gradient energy band distribution. Furthermore, dual recycle of Exo III-assisted cDNA and PECCC redox greatly enhanced the amplification effect of the target, eliminating the common drawbacks of cumbersome manufacture and non-ideal sensitivity. Taking advantage of prominent photoactive nanomaterials and target-driven dual signal amplification strategies, a wide linearity range and desirable detection performance were achieved. It is anticipated that the developed split-type PEC sensor will set up new perspectives for the field of microfluidic paper-based analytical devices by developing full automation technology of a paper chip, regulating the structure and composition of nanomaterials on cellulose paper, designing cascaded signal amplification, etc.

ASSOCIATED CONTENT

Supporting Information

The Supporting Information is available free of charge at https://pubs.acs.org/doi/10.1021/acs.analchem.1c04259.

Materials and reagents, design of the paper-based sensing platform, incubation and detection time optimization, analytical performance of the designed biosensor, recovery measurement, the illustration of the as-designed paper-based sensing platform, the SEM images of In_2S_3/WO_3/Au-PWE and In_2S_3-P/WO_3/Au-PWE, the high-resolution XPS spectra of In_2S_3-P/WO_3/Au-PWE, characterizations of $ZnFe_2O_4$ octahedrons and PdAgNSs, the $I-t$ curve of the electrode treated with FcA/AA/TCEP, analytical performances comparison of different methods, and detection of OTA in red wine samples (PDF)

AUTHOR INFORMATION

Corresponding Authors

Li Li − *School of Chemistry and Chemical Engineering, University of Jinan, Jinan 250022, P. R. China;* orcid.org/0000-0003-2849-5984; Email: chm_lili@ujn.edu.cn

Jinghua Yu − *School of Chemistry and Chemical Engineering, University of Jinan, Jinan 250022, P. R. China;* orcid.org/0000-0001-5043-0322; Phone: +86-531-82767040; Email: ujn.yujh@gmail.com

Authors

Xiaoran Tan − *School of Chemistry and Chemical Engineering, University of Jinan, Jinan 250022, P. R. China*

Haihan Yu − *School of Chemistry and Chemical Engineering, University of Jinan, Jinan 250022, P. R. China*

Bing Liang − *School of Chemistry and Chemical Engineering, University of Jinan, Jinan 250022, P. R. China*

Mengting Han − *School of Chemistry and Chemical Engineering, University of Jinan, Jinan 250022, P. R. China*

Shenguang Ge − *Institute for Advanced Interdisciplinary Research, University of Jinan, Jinan 250022, P. R. China;* orcid.org/0000-0002-0537-6491

Lina Zhang − *Shandong Provincial Key Laboratory of Preparation and Measurement of Building Materials, University of Jinan, Jinan 250022, P. R. China*

Lin Li − *School of Chemistry and Chemical Engineering, University of Jinan, Jinan 250022, P. R. China*

Complete contact information is available at: https://pubs.acs.org/10.1021/acs.analchem.1c04259

Notes

The authors declare no competing financial interest.

https://doi.org/10.1021/acs.analchem.1c04259
Anal. Chem. 2022, 94, 1705−1712

■ ACKNOWLEDGMENTS

This work was financially supported by the Taishan Scholars Program, the Case-by-Case Project for Top Outstanding Talents of Jinan, the National Natural Science Foundation of China (21874055), the project of "20 items of University" of Jinan (2018GXRC001), and the Excellent Youth Innovation Team in Universities of Shandong (2019KJC016).

■ REFERENCES

(1) Cai, J.; Hao, C.; Sun, M.; Ma, W.; Xu, C.; Kuang, H. *Small* **2018**, *14*, 1703931.
(2) Tang, J.; Huang, Y.; Zhang, C.; Liu, H.; Tang, D. *Biosens. Bioelectron.* **2016**, *86*, 386−392.
(3) Deore, P. S.; Gray, M. D.; Chung, A. J.; Manderville, R. A. *J. Am. Chem. Soc.* **2019**, *141*, 14288−14297.
(4) Xu, G.; Zhao, J.; Liu, N.; Yang, M.; Zhao, Q.; Li, C.; Liu, M. *Nucleic Acids Res.* **2019**, *47*, 5963−5972.
(5) Wang, Z.; Yu, H.; Han, J.; Xie, G.; Chen, S. *Chem. Commun.* **2017**, *53*, 9926−9929.
(6) Lu, Z.; Chen, X.; Hu, W. *Sens. Actuators, B* **2017**, *246*, 61−67.
(7) Wang, X.; Park, S. G.; Ko, J.; Xiao, X.; Giannini, V.; Maier, S. A.; Kim, D. H.; Choo, J. *Small* **2018**, *14*, 1801623.
(8) Wang, Y.; Song, W.; Zhao, H.; Ma, X.; Yang, S.; Qiao, X.; Sheng, Q.; Yue, T. *Biosens. Bioelectron.* **2021**, *182*, 113171.
(9) Sun, H.; Dong, C.; Liu, Q.; Yuan, Y.; Zhang, T.; Zhang, J.; Hou, Y.; Zhang, D.; Feng, X. *Adv. Mater.* **2020**, *32*, 2002486.
(10) Cai, S.; Zuo, C.; Zhang, J.; Liu, H.; Fang, X. *Adv. Funct. Mater.* **2021**, *31*, 2100026.
(11) Zhang, G.; Zeng, J.; Yin, J.; Zuo, C.; Wen, P.; Chen, H.; Qiu, Y. *Appl. Catal., B* **2021**, *286*, 119902.
(12) Zhou, C.; Cui, K.; Liu, Y.; Hao, S.; Zhang, L.; Ge, S.; Yu, J. *Anal. Chem.* **2021**, *93*, 5459−5467.
(13) Ding, R.; Cheong, Y. H.; Ahamed, A.; Lisak, G. *Anal. Chem.* **2021**, *93*, 1880−1888.
(14) Bagheri, N.; Mazzaracchio, V.; Cinti, S.; Colozza, N.; Di Natale, C.; Netti, P. A.; Saraji, M.; Roggero, S.; Moscone, D.; Arduini, F. *Anal. Chem.* **2021**, *93*, 5225−5233.
(15) Chen, F. F.; Dai, Z. H.; Feng, Y. N.; Xiong, Z. C.; Zhu, Y. J.; Yu, Y. *ACS Nano* **2021**, *15*, 5355−5365.
(16) Gao, C.; Yu, H.; Zhang, L.; Zhao, Y.; Xie, J.; Li, C.; Cui, K.; Yu, J. *Anal. Chem.* **2020**, *92*, 2902−2906.
(17) Li, L.; Zhang, Y.; Yan, Z.; Chen, M.; Zhang, L.; Zhao, P.; Yu, J. *ACS Sens.* **2020**, *5*, 1482−1490.
(18) Li, L.; Shi, H.; Yu, H.; Tan, X.; Wang, Y.; Ge, S.; Wang, A.; Cui, K.; Zhang, L.; Yu, J. *Appl. Catal., B* **2021**, *292*, 120184.
(19) Yang, J.; Li, Y.; Guo, L.; Qiu, B.; Lin, Z. *Anal. Chem.* **2021**, *93*, 8370−8378.
(20) Yu, S.-Y.; Mei, L.-P.; Xu, Y.-T.; Xue, T.-Y.; Fan, G.-C.; Han, D.-M.; Chen, G.; Zhao, W.-W. *Anal. Chem.* **2019**, *91*, 3800−3804.
(21) Kim, J. H.; Won Yoon, J.; Kim, T.-H.; Jo, Y.-M.; Kim, J.-S.; Jeong, S.-Y.; Lee, J.-H. *Chem. Eng. J.* **2021**, *425*, 131496.
(22) Peng, B.; Zhang, Z.; Tang, L.; Ouyang, X.; Zhu, X.; Chen, L.; Fan, X.; Zhou, Z.; Wang, J. *Anal. Chem.* **2021**, *93*, 9129−9138.
(23) Szkoda, M.; Trzciński, K.; Trykowski, G.; Łapiński, M.; Lisowska-Oleksiak, A. *Appl. Catal., B* **2021**, *298*, 120527.
(24) Wang, J.; Jiang, L.; Liu, F.; Jia, M.; Liu, M.; Li, J.; Lai, Y. *Chem. Eng. J.* **2021**, *407*, 127195.
(25) Yuan, K. P.; Zhu, L. Y.; Yang, J. H.; Hang, C. Z.; Tao, J. J.; Ma, H. P.; Jiang, A. Q.; Zhang, D. W.; Lu, H. L. *J. Colloid Interface Sci.* **2020**, *568*, 81−88.
(26) Chen, X.; Zhang, W.; Zhang, L.; Feng, L.; Zhang, C.; Jiang, J.; Wang, H. *ACS Appl. Mater. Interfaces* **2021**, *13*, 25868−25878.
(27) Tian, W.; Chen, C.; Meng, L.; Xu, W.; Cao, F.; Li, L. *Adv. Energy Mater.* **2020**, *10*, 1903951.
(28) Wang, B.; Mei, L. P.; Ma, Y.; Xu, Y. T.; Ren, S. W.; Cao, J. T.; Liu, Y. M.; Zhao, W. W. *Anal. Chem.* **2018**, *90*, 12347−12351.
(29) Wang, B.; Xu, Y. T.; Lv, J. L.; Xue, T. Y.; Ren, S. W.; Cao, J. T.; Liu, Y. M.; Zhao, W. W. *Anal. Chem.* **2019**, *91*, 3768−3772.
(30) Yi, W.; Cai, R.; Xiang, D.; Wang, Y.; Zhang, M.; Ma, Q.; Cui, Y.; Bian, X. *Biosens. Bioelectron.* **2019**, *143*, 111614.
(31) Cao, J. T.; Wang, B.; Dong, Y. X.; Wang, Q.; Ren, S. W.; Liu, Y. M.; Zhao, W. W. *ACS Sens.* **2018**, *3*, 1087−1092.
(32) Shuai, H. L.; Huang, K. J.; Xing, L. L.; Chen, Y. X. *Biosens. Bioelectron.* **2016**, *86*, 337−345.
(33) Xing, Z.; Ju, Z.; Yang, J.; Xu, H.; Qian, Y. *Nano Res.* **2012**, *5*, 477−485.
(34) Zhou, Y.; Zhou, R.; Zhu, X.; Han, N.; Song, B.; Liu, T.; Hu, G.; Li, Y.; Lu, J.; Li, Y. *Adv. Mater.* **2020**, *32*, 2000992.
(35) Zhang, Y.; Lin, C.; Lin, Q.; Jin, Y.; Wang, Y.; Zhang, Z.; Lin, H.; Long, J.; Wang, X. *Appl. Catal., B* **2018**, *235*, 238−245.

https://doi.org/10.1021/acs.analchem.1c04259
Anal. Chem. 2022, 94, 1705−1712